Photo-Induced Halide Redistribution in 2D Halide Perovskite Lateral Heterostructures

Yanqi Luo,[1,2,8†] Shuchen Zhang,[3†] Jia-Shiang Chen,[4,5] Xuedan Ma,[4,5,6] Ke Ma,[3] Junjing Deng,[1] Yi Jiang,[1] Luxi Li,[1] Barry Lai,[1] Si Chen,[1] Sarah Wieghold,[1] and Letian Dou[3,7*]*

[1] *Advanced Photon Source, Argonne National Laboratory, Lemont, IL 60439*
[2] *Advanced Light Source, Lawrence Berkeley National Laboratory, Berkeley, CA 94720*
[3] *Davidson School of Chemical Engineering, Purdue University, West Lafayette, IN, 47907*
[4] *Center for Nanoscale Materials, Argonne National Laboratory, Argonne, IL 60439*
[5] *Center for Molecular Quantum Transduction, Northwestern University, Evanston, IL 60208*
[6] *Consortium for Advanced Science and Engineering, University of Chicago, Chicago, IL 60637*
[7] *Department of Chemistry, Purdue University, West Lafayette, IN, 47907*

*Corresponding authors. Email: yluo89@lbl.gov (Y.L), dou10@purdue.edu (L.D.)
† These authors contributed equally to this work.
[8] Lead contact

Summary. An improved understanding of the degradation pathways under external stimuli is needed to address stability challenges in two-dimensional (2D) perovskite semiconductor materials. In this study, *in-situ synchrotron* nanoprobe X-ray fluorescence (nano-XRF) is utilized to investigate the evolution of halide redistribution within various 2D halide perovskites (n = 1 to 3) lateral heterostructures under ultraviolet (UV) exposure. The results show that iodine experiences a loss in all cases, with the rate of change following the perovskite dimensionality monotonically. In contrast, bromine is relatively more stable than iodine in n = 2 and 3 heterostructures, with no significant change in total Br concentration but a visible amount of Br diffusion to the previously iodine-rich regime. Combining nano-XRF and X-ray absorption spectroscopy, we found a reduction of dimensionality in crystals with n > 1 after UV exposure, indicating significant structural reconfiguration beyond ion migration.

Introduction.

Lead halide perovskites have garnered significant interest as semiconducting materials due to their wide range of optoelectronic tunability and excellent performance, making them attractive for applications such as light-harvesting photovoltaics [1] and light-emitting diodes (LEDs).[2] Considerable progress has been made in developing perovskite tandem solar cells [3,4] and color-tunable LEDs spanning the UV-vis to near-IR spectrum [5–7] through various combinations and ratios of halide (I, Br, and Cl) mixing.[8,9] However, intrinsic photo- and operation-induced halide redistribution and segregation are prevalent in mixed halide perovskites, leading to the formation of photoinactive secondary phase in photovoltaics[10,11] and shifts of emission properties of LEDs.[12] The driving force for halide rearrangement is potentially due to a combination of high vacancy concentrations (10^{17} - 10^{20} cm^{-3}) and a low migration energy barrier of halide ions.[13,14]

Low-dimensional perovskites have demonstrated significant potential in mitigating degradation issues in perovskite materials by enhancing their intrinsic thermal/photo-stability and suppression of ionic migration.[15–19] Unlike the three-dimensional (3D) perovskites, Ruddlesden−Popper two-dimensional (2D) perovskites have layers of lead halide PbX_6 (X=I, Br and Cl) inorganic networks that are sandwiched by large monoammonium organic spacer cations, *L*, leading to chemical formula $L'_2A_{n-1}Pb_xX_{3n+1}$, where *n* defines the number of octahedral perovskite layers and reflects the dimensionality of perovskites.[15] Numerous research efforts have focused on understanding the thermal stability of dimensionality-dependent 2D perovskites that are synthesized using various types of organic spacers.[20,21] A recent calorimetric study revealed that monoammonium organic spacers exhibit better thermal and air stability compared

to the divalent/diammonium ones due to a negative enthalpy in the formation and strong distortions in the PbX_6 octahedra layers.[17] Moreover, we recently developed a variety of lateral and vertical heterostructures of 2D perovskites as diffusion couples and showed that bulky and right π-conjugated ligands are more effective in suppressing thermally induced halide inter-diffusion than conventional aliphatic ligands.[22,23]

These early studies indicate the influence of organic spacers on the thermal stability of low-dimensional perovskites and offer valuable guidance for selecting spacers to enhance device passivation and durability.[24] However, the effects of photoinduced redistribution / migration of halide ions within low-dimensional perovskites and relative stability between I / Br 2D perovskites are less explored.[25–27] Xiao et al. found that incorporating *n*-butylammonium (BA) spacer in Br-I mixed halide perovskite nanoparticles suppressed halide redistribution/segregation after 20 mins of 1-Sun irradiation.[28] Similar to thermal induced ion diffusion, a recent work shows that photo-induced phase segregation becomes negligible upon replacing BA with a phenethylammonium (PEA) spacer in n = 1 $PEA_2PbBr_2I_2$ perovskites.[29] However, most previous works relied on indirect measurements (e.g., tracked by absorption or photoluminescence) and on macroscopic samples without microscopic spatial resolution.

In this study, we monitor the evolution of halide redistribution within various dimensional PEA-based 2D crystals using *in-situ* nanoprobe X-ray fluorescence (nano-XRF) under continuous UV exposure in an inert environment. The 2D crystals have unique heterostructures initially, composed of I- and Br- rich regimes laterally. In crystals with n = 2 and 3, different from thermal-induced anionic diffusion, the iodine regime undergoes rapid sublimation, while Br is relatively stable and gradually diffuses/migrates to the previously I-rich regime upon UV irradiation. On the

other hand, the heterostructure with *n* = 1 remains stable with a small observable change of halide concentration. Further, in conjunction with nano-XRF composition mapping, X-ray absorption spectroscopy (XAS) indicates a reduction of dimensionality in the previously iodine-rich regime in crystals with *n* > 1 after UV exposure.

Result and Discussion.

Synchrotron-based hard X-ray nanoprobe is used to identify the spatial distribution of halides and understand their photostability in 2D perovskites under continuous UV irradiation, as shown in **Figure 1a**. During the nano-XRF measurements, a focused X-ray beam with 14 keV photon energy is used to excite the elemental characteristic XRF L- or K- emission lines of the major substituents in 2D perovskites, including I, Br, and Pb.[14,30] The raster XRF map provides elemental distribution with spatial resolution in a range of 80 to 250 nm, limited by the focused X-ray beam spot size. In addition, we positioned the crystals of interest in the X-ray beam path and introduced UV illumination for the *in-situ* nano-XRF experiment using a visible light microscope setup (detailed in Supplemental experimental procedures).

The PEA-based 2D crystals with varying dimensionality (*n* = 1 to 3) are used to investigate dimensionality-dependent ionic migration and photostability. The chosen 2D heterostructures crystals with distinguishable I- and Br- rich domains facilitate sensitive detection of halide redistribution either within or across these heterojunctions. Note that *n* = 1 crystal was prepared using sequential solvent evaporation method, while *n* = 2 and 3 heterostructures were synthesized via ion exchange (detailed in Supplemental experimental procedures). These 2D lateral heterostructures, with the formula of $PEA_2MA_{n-1}Pb_xX_{3n+1}$ and typical thickness in range of

48 to 300 nm (shown in **Figure S1**), were span on 200 nm thick SiN_x membrane substrates. The isolated I- and Br- regimes, which have distinct differences in the bandgap and emission properties, are easily identifiable using photoluminescence (PL) images shown in **Figure 1b**. The area-averaged PL spectra shown in **Figure 1c** illustrate that the Br-regimes exhibit blue PL emission with photons energies in a range of 400 to 500 nm, while I-regimes emit in red (> 600 nm) for $n > 1$ and green (510 nm) for $n = 1$ perovskites. The shift of PL peak positions agrees with the expected quantum confinement effect when changing the dimensionality from $n = 1$ to 3.[31,32] In addition to this optical method, an alternative approach to identify the two halide regimes is to directly detect the elemental concentration directly using nano-XRF. Within the selected 2D heterostructures, a similar halide distribution is observed (see column 1 in **Figure 2a-c** corresponding to Figure 1b). For instance, the regions of green and blue emitting PL in the $n = 1$ perovskite (*i.e.,* Figure 1b, *left*) are well-aligned with the I- and Br- regime detected in nano-XRF (*i.e.,* Figure 2a, column 1), respectively. Lateral heterostructures with $n > 2$ appear to have incomplete ionic exchange during material synthesis, which leads to a noticeable amount of residual Br in the iodine regime, as evidenced by nano-XRF. Considering the penetration length of the X-ray beam at 14 keV [30,33] substantially exceeds the typical thickness of the synthesized crystals, the nano-XRF signals can be interpreted as an approximate summation of elemental concentrations along the sample thickness.

2D perovskites with the lowest dimensionality ($n = 1$) show better photostability than $n = 2$ and 3 under continuous UV irradiation. The UV LED light source has a center wavelength of 365 nm with a power of 36 mW. The left-most column displays the initial XRF maps of the I:Pb and Br:Pb molar ratio in 2D heterostructures, followed by the change of halide concentration relative

to the initial values based on the chronological sequence of light soaking duration shown in Figure 2a to c. The relative change XRF maps use a three-color gradient color bar, where red, white, and blue pixels indicate increasing, no change, and decreasing halide concentration, respectively.

Compared with 2D perovskite with n=1, photoinduced iodine sublimation and sequential bromine migration are clearly observed in *n* = 2 and 3 heterostructures. The initial iodine regimes experience rapid concentration loss upon UV exposure, with the visible change of I:Pb in 2 min for *n* = 3 perovskites. In contrast, the iodine remains relatively stable in *n* = 1 crystals, regardless of whether they were prepared using solvent evaporation (as shown in Figure 2a) or the anion exchange method (see **Figure S2**). The sublimation of iodine results in the creation of halide vacancies, which in turn enable the migration of mobile Br- ions into the sublimated regions, traversing the heterostructure boundary. The concern of X-ray beam-induced halide redistribution is resolved using another *n* = 3 crystal on the same substrate, in which iodine concentration remains unchanged after three consecutive nano-XRF scans, but varies when UV illumination is on, confirming the observed halide redistribution is initiated by UV rather than X-ray photons (shown in **Figure S3)**. Additionally, the observed halide redistribution is attributed to photophysical processes rather than a light-induced thermal effect, given that the estimated temperature change is 5 K or less during the initial 20 minutes of the light soaking experiment (as shown in **Figure S4**). The estimation is established in a worst-case scenario, where no heat transfer within the samples due to their ultra-low thermal conductivity[34] and incident heat flux is assumed to be equivalent to the energy absorbed by the 2D perovskites.

To quantitatively evaluate the migration of Br^- and loss of iodine, **Figure 2d-e** illustrates the relative changes in the average I:Pb and Br:Pb atomic ratio within the initial iodine-rich regimes.

The rate of iodine change varies and follows the order of the perovskite dimensionality monotonically. In *n* = 3 perovskite, the reduction of iodine concentration follows an exponential decay, suggesting the presence of a high-order degradation reaction under UV exposure. Conversely, perovskites with *n* = 2 exhibit a slower rate of iodine loss than *n* = 3, while *n* = 1 shows a profile that is close to a plateau. In contrast, the concentration of Br in the entire 2D heterostructures maintains relatively unchanged during UV exposure, as shown in **Figure S5**. However, the spatial distribution of Br varies during UV exposure within the heterostructures with *n* > 1. As the spatial nano-XRF maps illustrated in **Figure 2**, Br migration is likely driven by the presence of iodine vacancies, and thus results in a gradual accumulation of Br in the iodine sublimated area. The area-averaged Br:Pb atomic ratio has a 2 to 5% relative increment compared to the initial Br concentration in the given region. As expected, the ionic migration impacts the features of PL emission spectrum, which could be used to explain the PL intensity enhancement in the area where Br accumulation is expected in *n* = 2 heterostructures shown in **Figure S6**. The halide redistribution process appears to be irreversible. Iodine doesn't recover, but continuous Br diffusion occurs after storing UV exposed n = 3 perovskites in the dark for 10 hours shown in **Figure S7**.

Despite that *n* = 1 heterostructure displays weak preferential ionic migration of halide mixing across the heterostructure and iodine concentration remains relatively stable, it is worth noting that Br concentration gradually decreases, resulting in vacancy-mediated iodine diffusion over a prolonged period of continuous UV exposure, as shown in Figure 2a and e. The enhanced stability of iodine in *n* = 1 structures can be rationalized from both thermodynamic and photophysical perspectives. Decreased enthalpy of formation (ΔH) in structures with smaller n

values and light-induced decomposition of MA^+ are likely the key contributors to iodine sublimation observed in n = 2 and 3 heterostructures.[15,35] Conversely, the lower stability of Br in *n* = 1 perovskite could be associated with a decrease in lattice rigidity and an increase in lattice distortion and mismatch between the inorganic perovskite layer and organic layer.[36]

Compared to the typical 2D thin films utilized in devices, the chosen 2D heterostructures serve as a simplified material system. This aids in the unambiguous understanding of dimensionality-dependent halide migration while excluding the contributions from grain boundaries. However, it's essential to consider the differing time- and length- scales of halide redistribution and the relevant degradation mechanisms between the two systems. Drawing from a recent quantitative secondary ion mass spectroscopy (SIMS) study on 3D halide perovskites, it's known that ion migration/diffusion within grains is slow but accelerates along grain boundaries.[37] This difference results in diffusion coefficients that can vary typically by 2 to 4 orders of magnitude at room temperature. Consequently, we would expect halide diffusion to occur more rapidly in 2D thin films than in the heterostructure crystals.

In addition to the evolution of halide distribution, X-ray absorption spectroscopy (XAS) provides further insights into the change of atomic structure via coordination in materials.[38] Specifically, XAS near the Br-K edge can qualitatively reveal the local atomic structure and related dimensionality. Moreover, probing the XAS signal in the area with the occurrence of iodine sublimation and Br diffusion, as shown in **Figure 3a**, can uncover the mechanism of photo-induced degradation. For example, before UV exposure, the rising edge of *n* = 1 is higher than *n* = 3 perovskites, suggesting a higher binding energy for Br ionization in lower dimensional materials, illustrated in overlaid XAS spectra and their first-order derivative. This trend matches

the previously reported size/quantum effect on XAS in diamond and Si nanocrystals.[39,40] After photo-induced degradation, the rising edge of *n* = 3 perovskite shifts to high energy toward the energy edge of pristine *n* = 1 PEA-Br perovskites. Meanwhile, *n* = 1 shows rising edge shifts to lower energy. This shift is likely attributable to the local formation of $PbBr_2$, which could occur after repeated X-ray and UV exposure,[14] and has an energy onset lower than that of halide perovskites.[38]

Through the use of nano-XRF and XAS, this study has revealed a possible degradation pathway for PEA-based 2D lateral heterostructures. **Figure 3b** schematically illustrates the observed changes in halide redistribution. Unlike *n*-butylammonium mixed halide perovskites ($BA_2PbBr_2I_2$) thin films,[41] where halide mixing was recently reported, this study observed iodine sublimation and sequential bromide migration when *n* > 1. The rate of iodine reduction increases with higher material dimensionality, suggesting the occurrence of photochemical redox reactions, involving photo-oxidation of iodide to molecular iodine, along with evaporation and decomposition of methylammonium cations to amine and water molecules,[25] which can easily escape from systems. Considering higher dimension perovskites have lower exciton binding energy and longer carrier lifetime,[42,43] the relationship between the rate of change and material dimensionality can be viewed and governed by the number of photogenerated free carriers during light absorption. The sublimation of iodine leaves iodine vacancies behind, which serves as the primary driving force behind vacancy-mediated halide migration. This allows the sequential migration of mobile bromide ions, leading to the formation of Br-rich mixed halide perovskites. Despite the role of increased vacancy concentration, the intrinsic electric field imposed by charge carriers has been suggested to play a role in ionic diffusion.[14] In $MAPb(Br_xI_{1-}$

$_x)_3$ perovskites, iodine perovskites often exhibit a larger absorption coefficient than their Br counterparts.[44] This disparity could potentially generate a built-in electric field, originating from the iodine regime and directed towards the Br regime, due to the unequal distribution of charge carriers laterally, which promotes and encourage ionic diffusion of Br^- with a direction against the electric field.[14] Sequentially, the movement and redistribution of the halide ions could lead to structural damage and rearrangement, yielding the transition from higher to lower dimensional perovskites, as indicated in XAS. The photo-induced dimensionality reduction is also observed optically in **Figure S8**, where several peak maxima appear on a PL spectrum measured on a long-lived 2D crystal after UV and X-ray radiation exposure. The shift in the emission spectrum complicates the evaluation of the contribution from self-trapped carriers in the crystal lattice (strong-coupled polarons), which typically accompanies a red-shift in PL.[45] Further studies are required to quantify the relative contribution and significance of each mechanism driving halide redistribution. Continued detailed studies of ionic migration are crucial as ion migration can drastically change the optoelectronic properties and, subsequently, the overall performance output of perovskites. Overall, these results suggest that 2D perovskites degrade through a different mechanism compared to under heat and reaffirm the importance of lowering halide vacancy concentration for decreasing ion migration and degradation in halide perovskites.

Conclusion. In summary, we systematically investigated dimensionality-dependent halide migration and photo-stability in PEA-based 2D perovskite lateral structures. Our *in-situ* nano-XRF and XAS studies reveal halide distribution and dimensionality reduction under continuous UV

exposure. We find that 2D perovskites with Br substituent have better photostability than iodine ones for the same *n* number. Although the lowest dimension (*n* = 1) remains stable, photo-induced iodine sublimation and sequential bromide diffusion are observed in *n* = 2 and 3 perovskites. The link between halide stability and structural dimensionality makes it clear that controlling crystal chemistry is paramount. Possible strategies to enhance 2D perovskite stability without compromising the optoelectronic performance include partially substituting less stable iodine with bromide and replacing conventional organic spacers with more bulky and hydrophobic ones. Future investigations are required to understand the interaction of organic spacers with multiple external stimuli (e.g., heat, light, and electrical bias) and the relevant mechanism of ionic transport in low-dimensional perovskites for the full realization of their potential in optoelectronic devices.

Experimental Procedures

Detailed Materials and Methods can be found in the Supplemental experimental procedures.

Resource Availability

Lead Contact

Further information should be directed to the Lead Contact, Yanqi Luo (yluo89@lbl.gov).

Materials Availability

This study did not generate new unique materials.

Data and Code Availability

Data and code are available at DOI: 10.5281/zenodo.8201636

Acknowledgments

This research used resources of both the Center for Nanoscale Materials and the Advanced Photon Source, a U.S. Depart of Energy (DOE) office of Science User Facility operated for the DOE Office of Science by Argonne National Laboratory under Contract No. DE-AC02-06CH11357. Y.L, S.C., S.W. acknowledge the support of ANL Laboratory Directed Research and Development PRJ1008073 and PRJ1009689. S.Z. and L.D. acknowledge the support of National Science Foundation under Award No. 2143568-DMR. J.-S. Chen acknowledges support from the Center

for Molecular Quantum Transduction, an Energy Frontier Research Center funded by the U.S. Department of Energy, Office of Science, Office of Basic Energy Sciences, under award no. DE-SC0021314.

Author Contributions.

Y.L., S.Z, and L.D. conceived the idea and designed the experiments; S.Z. and L.D. contributed to the fabrication of the lateral heterostructures; Y.L., S.C., and S.W. were involved in the *in-situ* nano-XRF and XAS measurement; J.S.C. and X.M. performed the *in-situ* PL measurements; S.Z. and K.M. performed the AFM and steady-state PL characterization; J.D., Y.J. L.L., B.L., and S.C. provided beamline support at 2ID at APS for all synchrotron measurements; Y.L., S.Z., J.S.C., X.M., S.W., and L.D. wrote the manuscript. All authors were involved in reviewing the manuscript.

Declaration of interests

The authors declare no competing interests.

References

1. Correa-Baena, J.P., Luo, Y., Brenner, T.M., Snaider, J., Sun, S., Li, X., Jensen, M.A., Hartono, N.T.P., Nienhaus, L., Wieghold, S., et al. (2019). Homogenized halides and alkali cation segregation in alloyed organic-inorganic perovskites. Science *363*, 627–631. 10.1126/science.aah5065.
2. Na Quan, L., Ma, D., Zhao, Y., Voznyy, O., Yuan, H., Bladt, E., Pan, J., García de Arquer, F.P., Sabatini, R., Piontkowski, Z., et al. (2020). Edge stabilization in reduced-dimensional perovskites. Nat. Commun. *11*, 1–9. 10.1038/s41467-019-13944-2.
3. Xu, J., Boyd, C.C., Yu, Z.J., Palmstrom, A.F., Witter, D.J., Larson, B.W., France, R.M., Werner, J., Harvey, S.P., Wolf, E.J., et al. (2020). Triple-halide wide-band gap perovskites with suppressed phase segregation for efficient tandems. Science *367*, 1097–1104. 10.1126/science.aaz4639.
4. Lin, R., Xu, J., Wei, M., Wang, Y., Qin, Z., Liu, Z., Wu, J., Xiao, K., Chen, B., Park, S.M., et al. (2022). All-perovskite tandem solar cells with improved grain surface passivation. Nature *603*, 73–78. 10.1038/s41586-021-04372-8.
5. Pang, P., Jin, G., Liang, C., Wang, B., Xiang, W., Zhang, D., Xu, J., Hong, W., Xiao, Z., Wang, L., et al. (2020). Rearranging Low-Dimensional Phase Distribution of Quasi-2D Perovskites for Efficient Sky-Blue Perovskite Light-Emitting Diodes. ACS Nano *14*, 11420–11430. 10.1021/acsnano.0c03765.
6. Yang, X., Zhang, X., Deng, J., Chu, Z., Jiang, Q., Meng, J., Wang, P., Zhang, L., Yin, Z., and You, J. (2018). Efficient green light-emitting diodes based on quasi-two-dimensional composition and phase engineered perovskite with surface passivation. Nat. Commun. *9*, 2–9. 10.1038/s41467-018-02978-7.
7. Xu, W., Hu, Q., Bai, S., Bao, C., Miao, Y., Yuan, Z., Borzda, T., Barker, A.J., Tyukalova, E., Hu, Z., et al. (2019). Rational molecular passivation for high-performance perovskite light-emitting diodes. Nat. Photonics *13*, 418–424. 10.1038/s41566-019-0390-x.
8. Luo, Y., Aharon, S., Stuckelberger, M., Magaña, E., Lai, B., Bertoni, M.I., Etgar, L., and Fenning, D.P. (2018). The Relationship between Chemical Flexibility and Nanoscale Charge Collection in Hybrid Halide Perovskites. Adv. Funct. Mater. *28*. 10.1002/adfm.201706995.

9. Jacobsson, T.J., Hultqvist, A., García-Fernández, A., Anand, A., Al-Ashouri, A., Hagfeldt, A., Crovetto, A., Abate, A., Ricciardulli, A.G., Vijayan, A., et al. (2022). An open-access database and analysis tool for perovskite solar cells based on the FAIR data principles. Nat. Energy *7*, 107–115. 10.1038/s41560-021-00941-3.
10. Li, N., Luo, Y., Chen, Z., Niu, X., Zhang, X., Lu, J., Kumar, R., Jiang, J., Liu, H., Guo, X., et al. (2020). Microscopic Degradation in Formamidinium-Cesium Lead Iodide Perovskite Solar Cells under Operational Stressors. Joule *4*, 1743–1758. 10.1016/j.joule.2020.06.005.
11. Bai, Y., Huang, Z., Zhang, X., Lu, J., Niu, X., He, Z., Zhu, C., Xiao, M., Song, Q., Wei, X., et al. (2022). Initializing film homogeneity to retard phase segregation for stable perovskite solar cells. Science *378*, 747–754.
12. Yang, J.N., Song, Y., Yao, J.S., Wang, K.H., Wang, J.J., Zhu, B.S., Yao, M.M., Rahman, S.U., Lan, Y.F., Fan, F.J., et al. (2020). Potassium Bromide Surface Passivation on CsPbI3-xBrx Nanocrystals for Efficient and Stable Pure Red Perovskite Light-Emitting Diodes. J. Am. Chem. Soc. *142*, 2956–2967. 10.1021/jacs.9b11719.
13. Walsh, A., Scanlon, D.O., Chen, S., Gong, X.G., and Wei, S.H. (2015). Self-regulation mechanism for charged point defects in hybrid halide perovskites. Angew. Chemie - Int. Ed. *54*, 1791–1794. 10.1002/anie.201409740.
14. Luo, Y., Khoram, P., Brittman, S., Zhu, Z., Lai, B., Ong, S.P., Garnett, E.C., and Fenning, D.P. (2017). Direct Observation of Halide Migration and its Effect on the Photoluminescence of Methylammonium Lead Bromide Perovskite Single Crystals. Adv. Mater. *29*. 10.1002/adma.201703451.
15. Li, X., Hoffman, J.M., and Kanatzidis, M.G. (2021). The 2D halide perovskite rulebook: How the spacer influences everything from the structure to optoelectronic device efficiency. Chem. Rev. *121*, 2230–2291. 10.1021/acs.chemrev.0c01006.
16. Lin, Y., Bai, Y., Fang, Y., Wang, Q., Deng, Y., and Huang, J. (2017). Suppressed Ion Migration in Low-Dimensional Perovskites. ACS Energy Lett. *2*, 1571–1572. 10.1021/acsenergylett.7b00442.
17. Vasileiadou, E.S., Wang, B., Spanopoulos, I., Hadar, I., Navrotsky, A., and Kanatzidis, M.G. (2021). Insight on the Stability of Thick Layers in 2D Ruddlesden-Popper and Dion-Jacobson Lead Iodide Perovskites. J. Am. Chem. Soc. *143*, 2523–2536. 10.1021/jacs.0c11328.
18. Azmi, R., Ugur, E., Seitkhan, A., Aljamaan, F., Subbiah, A.S., Liu, J., Harrison, G.T., Nugraha, M.I., Eswaran, M.K., Babics, M., et al. (2022). Damp heat – stable perovskite solar cells with tailored-dimensionality 2D / 3D heterojunctions. Science *376*, 1–9.
19. Sidhik, S., Wang, Y., De Siena, M., Asadpour, R., Torma, A.J., Terlier, T., Ho, K., Li, W., Puthirath, A.B., Shuai, X., et al. (2022). Deterministic fabrication of 3D/2D perovskite bilayer stacks for durable and efficient solar cells. Science *377*, 1425–1430. 10.1126/science.abq7652.
20. Yu, H., Xie, Y., Zhang, J., Duan, J., Chen, X., Liang, Y., Wang, K., and Xu, L. (2021). Thermal and Humidity Stability of Mixed Spacer Cations 2D Perovskite Solar Cells. Adv. Sci. *8*, 1–10. 10.1002/advs.202004510.
21. Fiorentino, F., Albaqami, M.D., Poli, I., and Petrozza, A. (2022). Thermal- and Light-Induced Evolution of the 2D/3D Interface in Lead-Halide Perovskite Films. ACS Appl. Mater. Interfaces *14*, 34180–34188. 10.1021/acsami.1c09695.
22. Akriti, Shi, E., Shiring, S.B., Yang, J., Atencio-Martinez, C.L., Yuan, B., Hu, X., Gao, Y.,

Finkenauer, B.P., Pistone, A.J., et al. (2021). Layer-by-layer anionic diffusion in two-dimensional halide perovskite vertical heterostructures. Nat. Nanotechnol. *16*, 584–591. 10.1038/s41565-021-00848-w.

23. Akriti, Zhang, S., Lin, Z.Y., Shi, E., Finkenauer, B.P., Gao, Y., Pistone, A.J., Ma, K., Savoie, B.M., and Dou, L. (2021). Quantifying Anionic Diffusion in 2D Halide Perovskite Lateral Heterostructures. Adv. Mater. *33*, 1–11. 10.1002/adma.202105183.
24. Aharon, S., Ceratti, D.R., Jasti, N.P., Cremonesi, L., Feldman, Y., Potenza, M.A.C., Hodes, G., and Cahen, D. (2022). 2D Pb-Halide Perovskites Can Self-Heal Photodamage Better than 3D Ones. Adv. Funct. Mater. *32*. 10.1002/adfm.202113354.
25. Udalova, N.N., Fateev, S.A., Nemygina, E.M., Zanetta, A., Grancini, G., Goodilin, E.A., and Tarasov, A.B. (2022). Nonmonotonic Photostability of BA2MAn-1PbnI3 n+1 Homologous Layered Perovskites. ACS Appl. Mater. Interfaces *14*, 961–970. 10.1021/acsami.1c20043.
26. Zha, Y., Wang, Y., Sheng, Y., Wu, S., Zhang, J., Ma, K., Yang, L., Liu, C., Di, Y., and Gan, Z. (2022). Structural characterizations on the degradation of 2D organic-inorganic hybrid perovskites and its enlightenment to improved stability. Nanotechnology *33*. 10.1088/1361-6528/ac64ad.
27. Suchan, K., Just, J., Beblo, P., Rehermann, C., Merdasa, A., Mainz, R., Scheblykin, I.G., and Unger, E. (2023). Multi-Stage Phase-Segregation of Mixed Halide Perovskites under Illumination: A Quantitative Comparison of Experimental Observations and Thermodynamic Models. Adv. Funct. Mater. *33*. 10.1002/adfm.202206047.
28. Xiao, Z., Zhao, L., Tran, N.L., Lin, Y.L., Silver, S.H., Kerner, R.A., Yao, N., Kahn, A., Scholes, G.D., and Rand, B.P. (2017). Mixed-Halide Perovskites with Stabilized Bandgaps. Nano Lett. *17*, 6863–6869. 10.1021/acs.nanolett.7b03179.
29. Mathew, P.S., Dubose, J.T., Cho, J., and Kamat, P. V. (2021). Spacer Cations Dictate Photoinduced Phase Segregation in 2D Mixed Halide Perovskites. ACS Energy Lett. *6*, 2499–2501. 10.1021/acsenergylett.1c01015.
30. Kodur, M., Kumar, R.E., Luo, Y., Cakan, D.N., Li, X., Stuckelberger, M., and Fenning, D.P. (2020). X-Ray Microscopy of Halide Perovskites: Techniques, Applications, and Prospects. Adv. Energy Mater. *10*. 10.1002/aenm.201903170.
31. Zhang, L., Sun, C., He, T., Jiang, Y., Wei, J., Huang, Y., and Yuan, M. (2021). High-performance quasi-2D perovskite light-emitting diodes: from materials to devices. Light Sci. Appl. *10*. 10.1038/s41377-021-00501-0.
32. Katan, C., Mercier, N., and Even, J. (2019). Quantum and Dielectric Confinement Effects in Lower-Dimensional Hybrid Perovskite Semiconductors. Chem. Rev. *119*, 3140–3192. 10.1021/acs.chemrev.8b00417.
33. Luo, Y., Gamliel, S., Nijem, S., Aharon, S., Holt, M., Stripe, B., Rose, V., Bertoni, M.I., Etgar, L., and Fenning, D.P. (2016). Spatially heterogeneous chlorine incorporation in organic-inorganic perovskite solar cells. Chem. Mater. *28*. 10.1021/acs.chemmater.6b02065.
34. Giri, A., Chen, A.Z., Mattoni, A., Aryana, K., Zhang, D., Hu, X., Lee, S.H., Choi, J.J., and Hopkins, P.E. (2020). Ultralow thermal conductivity of two-dimensional metal halide perovskites. Nano Lett. *20*, 3331–3337. 10.1021/acs.nanolett.0c00214.
35. Myae Soe, C.M., Nagabhushana, G.P., Shivaramaiah, R., Tsai, H., Nie, W., Blancon, J.C., Melkonyan, F., Cao, D.H., Traoré, B., Pedesseau, L., et al. (2019). Structural and thermodynamic limits of layer thickness in 2D halide perovskites. Proc. Natl. Acad. Sci. U.

S. A. *116*, 58–66. 10.1073/pnas.1811006115.
36. Vasileiadou, E.S., Hadar, I., Kepenekian, M., Even, J., Tu, Q., Malliakas, C.D., Friedrich, D., Spanopoulos, I., Hoffman, J.M., Dravid, V.P., et al. (2021). Shedding light on the stability and structure-property relationships of two-dimensional hybrid lead bromide perovskites. Chem. Mater. *33*, 5085–5107. 10.1021/acs.chemmater.1c01129.
37. Ghasemi, M., Guo, B., Darabi, K., Wang, T., Wang, K., Huang, C.W., Lefler, B.M., Taussig, L., Chauhan, M., Baucom, G., et al. (2023). A multiscale ion diffusion framework sheds light on the diffusion–stability–hysteresis nexus in metal halide perovskites. Nat. Mater. *22*, 329–337. 10.1038/s41563-023-01488-2.
38. Drisdell, W.S., Leppert, L., Sutter-Fella, C.M., Liang, Y., Li, Y., Ngo, Q.P., Wan, L.F., Gul, S., Kroll, T., Sokaras, D., et al. (2017). Determining Atomic-Scale Structure and Composition of Organo-Lead Halide Perovskites by Combining High-Resolution X-ray Absorption Spectroscopy and First-Principles Calculations. ACS Energy Lett. *2*, 1183–1189. 10.1021/acsenergylett.7b00182.
39. van Buuren, T., Dinh, L.N., Chase, L.L., Siekhaus, W.J., and Terminello, L.J. (1998). Changes in the electronic properties of si nanocrystals as a function of particle size. Phys. Rev. Lett. *80*, 3803–3806. 10.1103/PhysRevLett.80.3803.
40. Ley, L., Ristein, J., and Graupner, R. (2000). Quantum confinement effect in diamond nanocrystals studied by X-ray-absorption spectroscopy. Phys. Rev. Lett. *84*, 5679. 10.1103/PhysRevLett.84.5679.
41. Mathew, P.S., Szabó, G., Kuno, M., and Kamat, P. V. (2022). Phase Segregation and Sequential Expulsion of Iodide and Bromide in Photoirradiated Ruddlesden-Popper 2D Perovskite Films. ACS Energy Lett. *7*, 3982–3988. 10.1021/acsenergylett.2c02026.
42. Seitz, M., Magdaleno, A.J., Alcázar-Cano, N., Meléndez, M., Lubbers, T.J., Walraven, S.W., Pakdel, S., Prada, E., Delgado-Buscalioni, R., and Prins, F. (2020). Exciton diffusion in two-dimensional metal-halide perovskites. Nat. Commun. *11*, 1–8. 10.1038/s41467-020-15882-w.
43. Rahil, M., Ansari, R.M., Ahmad, S., and Islam, S.S. (2023). Nanostructured Ruddlesden–Popper-Layered Lead Bromide Perovskites with Stable and Selected Wavelength for Photodetection Applications. ACS Appl. Nano Mater. 10.1021/acsanm.2c05092.
44. Hoke, E.T., Slotcavage, D.J., Dohner, E.R., Bowring, A.R., Karunadasa, H.I., and McGehee, M.D. (2015). Reversible photo-induced trap formation in mixed-halide hybrid perovskites for photovoltaics. Chem. Sci. *6*, 613–617. 10.1039/c4sc03141e.
45. Liu, E., van Baren, J., Lu, Z., Taniguchi, T., Watanabe, K., Smirnov, D., Chang, Y.C., and Lui, C.H. (2021). Exciton-polaron Rydberg states in monolayer MoSe2 and WSe2. Nat. Commun. *12*, 1–8. 10.1038/s41467-021-26304-w.

Main figure title and legends.

Figure 1. Schematic of i*n-situ* nanoprobe X-ray fluorescence (nano-XRF) measurement and photoluminescence (PL) Analysis of Halide Redistribution in 2D Perovskite Heterostructures. (a) Schematic of the *in-situ* (nano-XRF) setup, allowing continuous UV illumination on the samples while mapping the evolution of halide redistribution using a 14 keV focused X-ray probe. (b) PL

images and (c) overlaid area-averaged PL spectra of PEA-based 2D lateral heterostructures, from *n* = 1 to 3. The as-prepared heterostructures have isolated I and Br regimes, where Br regimes have PL emission indicated in blue (400-500 nm) for all *n* dimensions, while I regime emits in red (> 600 nm) for *n* > 1 and green (510 nm) for *n* = 1. The PL measurement was taken using a 375 nm laser with 0.3 mW power. All the scale bars are 10 µm.

Figure 2. Nanoprobe X-ray fluorescence (nano-XRF) measurement of the changes in halide distribution in PEA-based 2D heterostructures under UV irradiation. (a) to (c) are the I and Br distribution for heterostructures with *n* = 1 to 3. The initial halide distribution without UV irradiation is shown in the leftmost column. The remaining columns display the change in halide distribution, with respect to the initial distribution, as a function of exposure duration. The gray color contours represent the boundaries of the heterostructures. Panels (d) and (e) show the average change in I:Pb and Br:Pb ratio, respectively, in initial iodine regime as a function of time. All scale bars are 5 µm.

Figure 3. X-ray absorption spectroscopy (XAS) analysis and proposed degradation mechanism of 2D perovskite heterostructures after UV exposure. (a) Overlaid XAS spectra and their first-order derivative for *n* = 1 and 3 perovskites before and after UV irradiation. (b) A proposed degradation schematic in the 2D perovskite lateral heterostructures after UV irradiation.

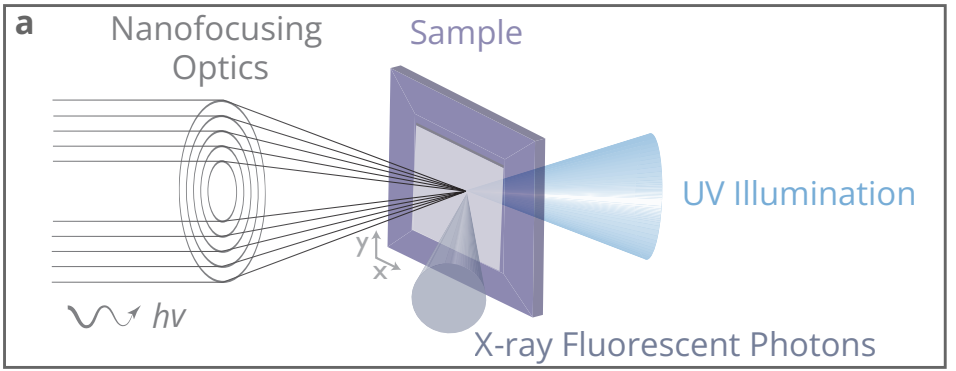
a
Nanofocusing Optics
Sample
UV Illumination
y
x
hv
X-ray Fluorescent Photons

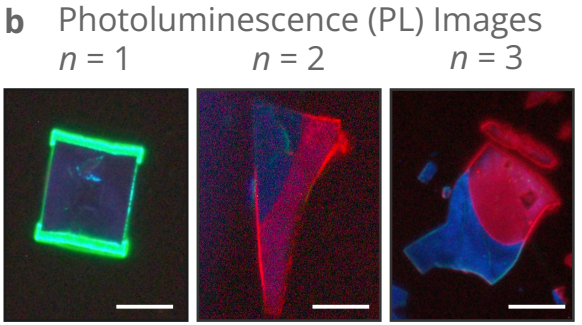
b
Photoluminescence (PL) Images
n = 1
n = 2
n = 3

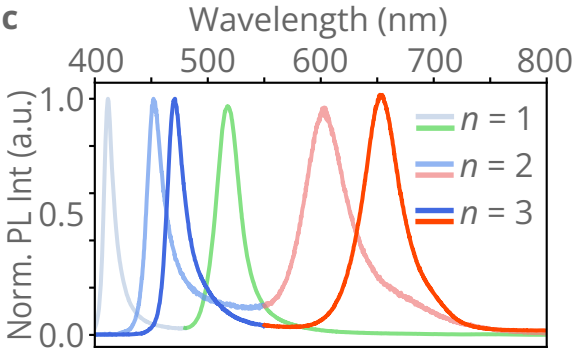
c
Wavelength (nm)
400
500
600
700
800
Norm. PL Int (a.u.)
1.0
0.5
0.0
n = 1
n = 2
n = 3

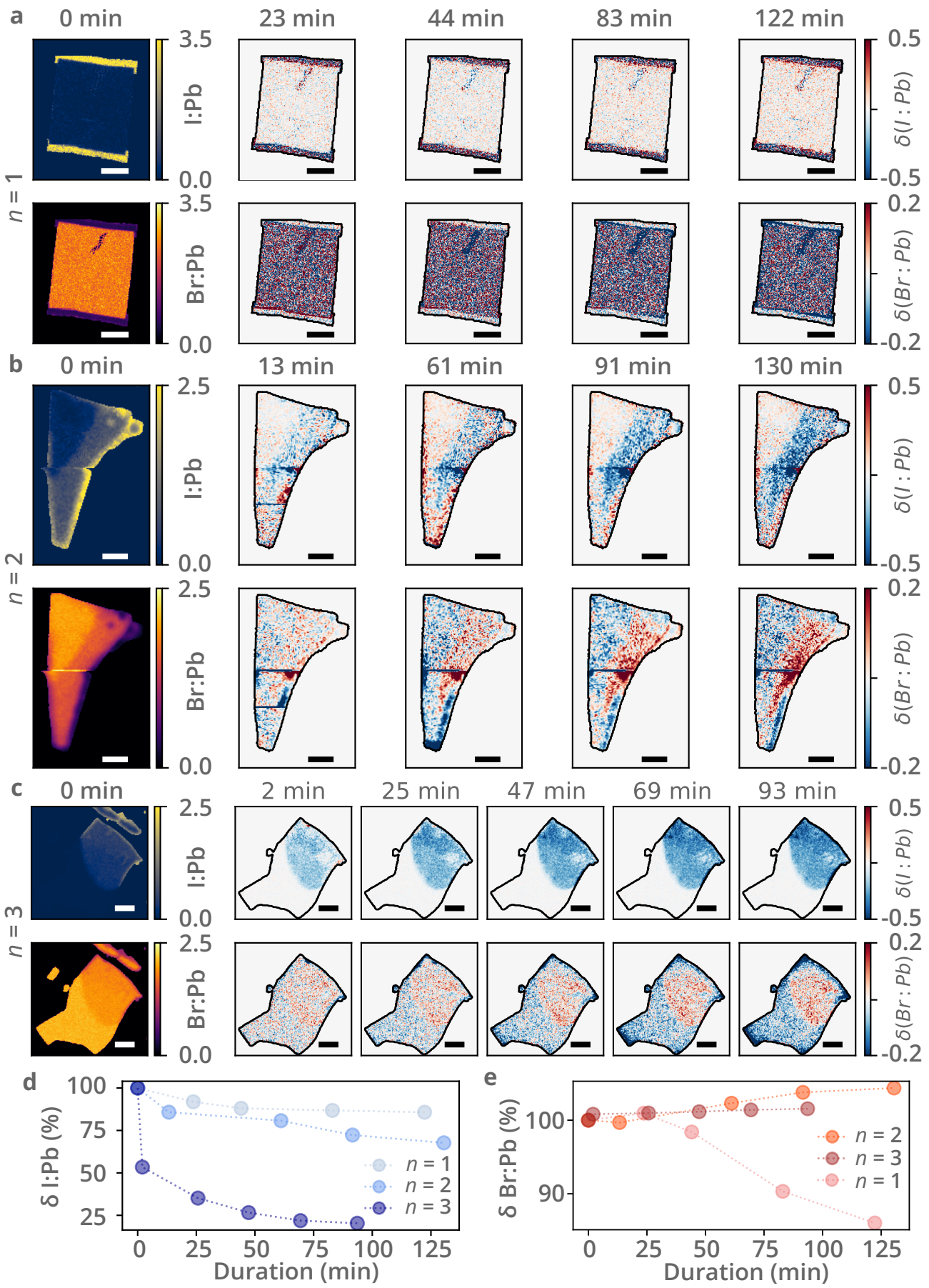
a
0 min
23 min
44 min
83 min
122 min
n = 1
I:Pb
Br:Pb
3.5
0.0
0.5
-0.5
0.2
-0.2
δ(I : Pb)
δ(Br : Pb)
b
0 min
13 min
61 min
91 min
130 min
n = 2
2.5
c
0 min
2 min
25 min
47 min
69 min
93 min
n = 3
d
δ I:Pb (%)
100
75
50
25
0
25
50
75
100
125
Duration (min)
n = 1
n = 2
n = 3
e
δ Br:Pb (%)
100
90

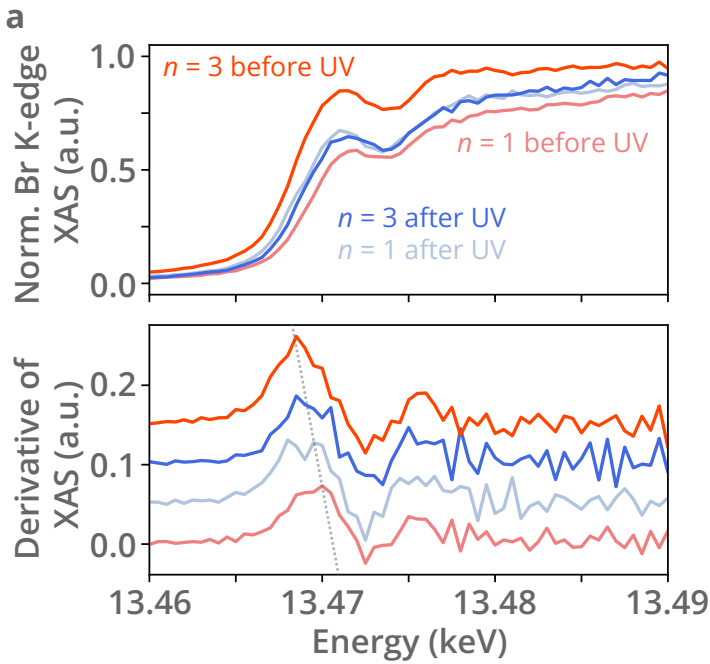
a
Norm. Br K-edge XAS (a.u.)
1.0
0.5
0.0
n = 3 before UV
n = 1 before UV
n = 3 after UV
n = 1 after UV
Derivative of XAS (a.u.)
0.2
0.1
0.0
13.46
13.47
13.48
13.49
Energy (keV)

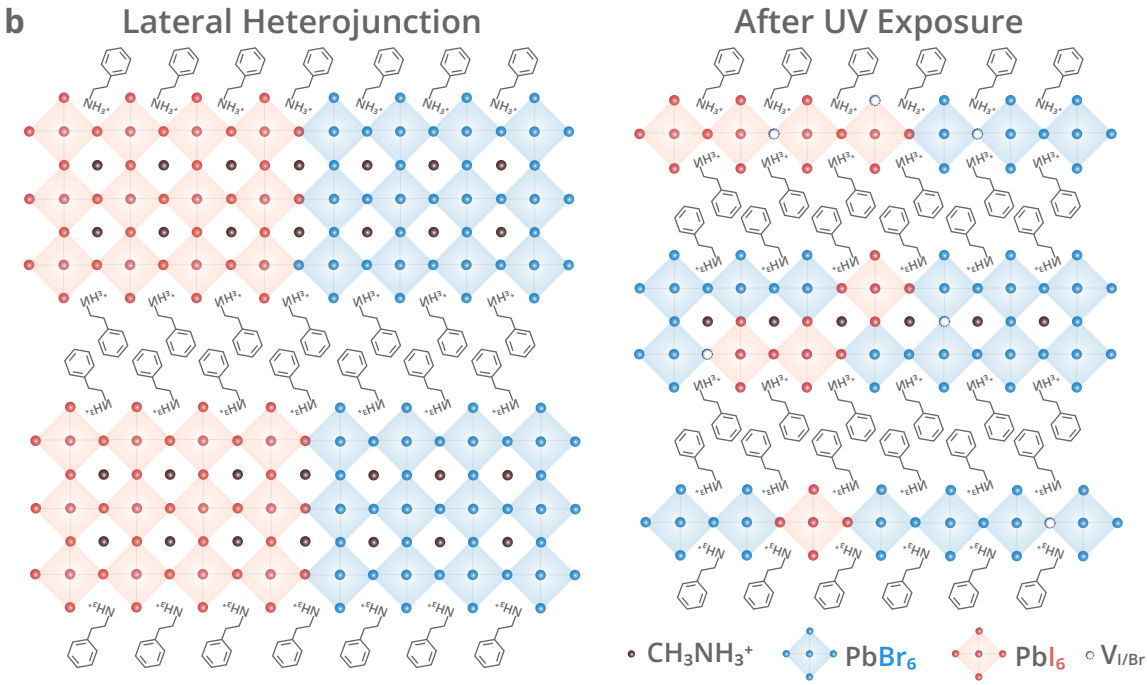
b
Lateral Heterojunction
After UV Exposure
CH3NH3+
PbBr6
PbI6
VI/Br

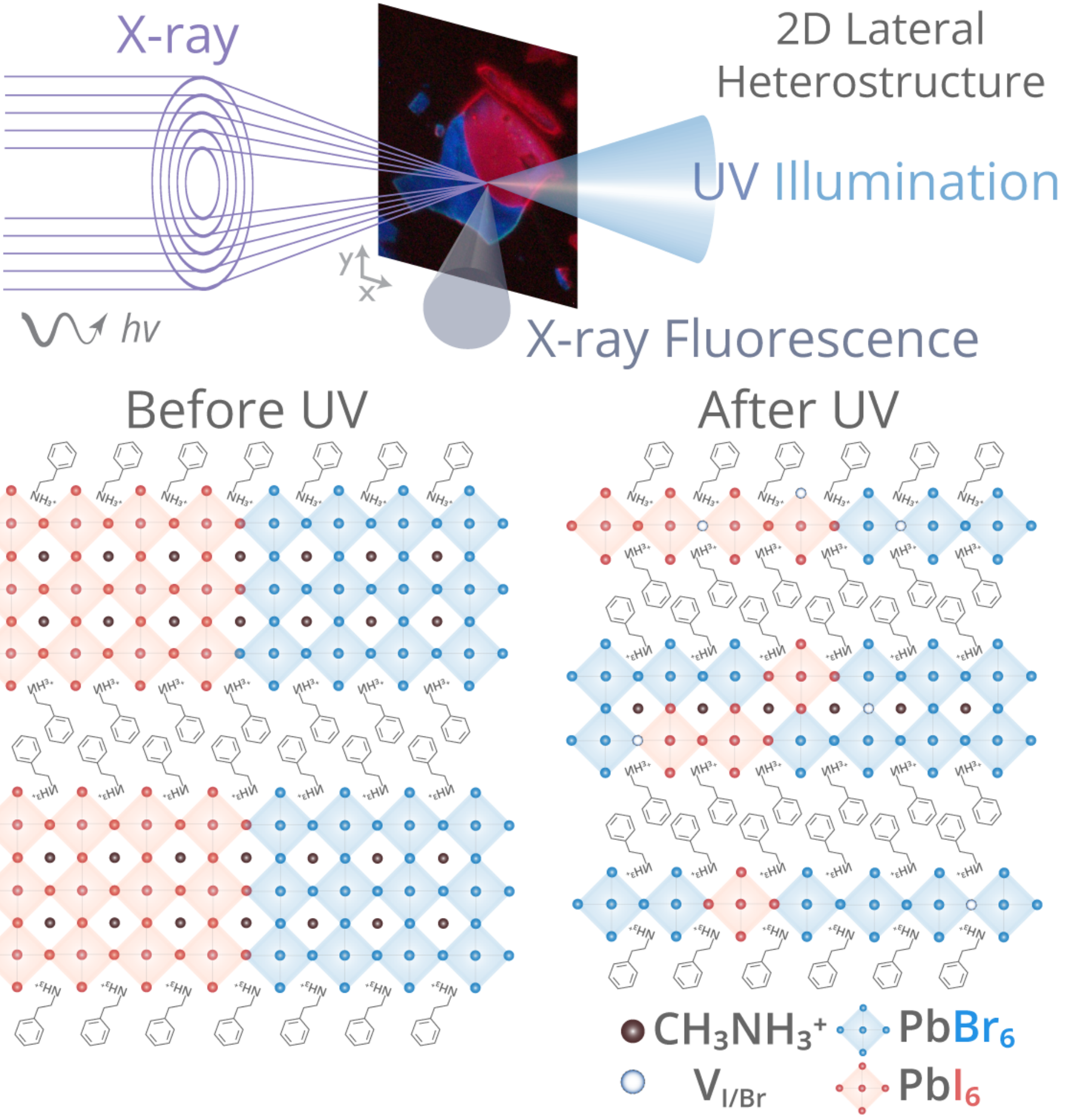
X-ray
2D Lateral Heterostructure
UV Illumination
hv
y
x
X-ray Fluorescence
Before UV
After UV
$CH_3NH_3^+$
$PbBr_6$
$V_{I/Br}$
PbI_6